RGNZ/MGPB

Application of the GMR permeability method to artificial geometries and micro-CT rock samples

Rudarsko-geološko-naftni zbornik
(The Mining-Geology-Petroleum Engineering Bulletin)
DOI: 10.17794/rgn.2026.5.6

Original scientific paper

Marko Gaćina[1]*, Domagoj Vulin[2]
[1] *INA-industrija nafte d.d., Av. Većeslava Holjevca 10, Zagreb, Croatia.*
[2] *University of Zagreb Faculty of Mining, Geology and Petroleum Engineering, Pierottijeva 6, Zagreb, Croatia.*

Abstract
Permeability in porous media is controlled by complex interactions between pore morphology, topology with pore connectivity, and flow-path constrictions across multiple spatial scales. To address this, we developed and tested a geometric mean radius (GMR) permeability method on both idealized and micro-CT derived pore geometries. The GMR workflow treats the segmented pore space as a sequence of cross-sections orthogonal to a prescribed flow direction, computes pore scale hydraulic radii from area and perimeter and combines them into a geometric mean radius along connected flow paths. Serial and parallel flow relations are then used to propagate local conductance through parent–child pore connections, accounting for pore branching, merging, and tortuous flow paths.
Controlled tube-like models are used to isolate the effects of pore roughness, cross-sectional shape complexity, flow-path constrictions, and network branching. Permeability predictions are evaluated for both simple geometries as well as real rock samples by using OpenLB and solvers found in Pergeos software.
Additional geometric analysis shows that weighted shape factor and coordination number correlate systematically with both permeability and the performance of the GMR model. Overall, the results demonstrate that GMR provides a computationally efficient and geometrically interpretable alternative to full pore scale flow simulation when applied within a clearly defined range of connectivity and resolution.

Keywords:
permeability; PNM; pore network geometry; hydraulic radius; geometric mean radius

1. Introduction

Permeability in natural rocks emerges from an interplay of complex pore shapes and pore networks that extend from nanometer-scale pores to millimeter-scale fractures. At the pore scale, the void space is highly irregular, with rough walls, non-circular cross-sections, and intricate splitting and merging of flow paths. Pore morphology (geometry of individual pores and throats) and pore topology (connectivity, coordination number, and loop structure) together control how easily fluids move through the porous medium. Their combined influence at different scales complicates permeability prediction, particularly when representative elementary volumes must span hundreds to thousands of voxels to capture the relevant heterogeneity and pore-space organization (**Berg, 2014**). Detailed pore morphology and topology cannot, in general, be inferred uniquely from bulk metrics such as porosity or specific surface area alone, because distinct pore spaces with identical porosity can exhibit markedly different permeability (**Hommel et al., 2018; Dullien, 1992**).

The conceptual origins of pore network modelling lie in early capillary bundle and effective-medium permeability descriptions, such as the Kozeny–Carman framework, which relate permeability to porosity, specific surface area, and tortuosity *via* simplified geometric assumptions (**Kozeny, 1927; Carman, 1937; Zakirov, 2020; Rehman et al., 2024**). While these classical relations remain influential, their empirical "constants" represent lumped correction factors that absorb unresolved geometric complexity, including pore shape irregularity, constriction losses, and connectivity effects (**Vincens et al., 2015; Li et al., 2024**).

Despite its widespread use, the Kozeny–Carman approach frequently overestimates permeability by an order of magnitude due to its insensitivity to dead-end pores, pore connectivity, and throat constrictions (**Walker & Glover, 2010**). This fundamental limitation has driven the development of physics-based alternatives that explicitly account for pore network connectedness. The RGPZ (Revil–Glover–Pezard–Zamora) framework addresses these deficiencies by incorporating formation factor and cementation exponent to capture connectivity

* Corresponding author: Marko Gaćina
e-mail address: marko.gacina@ina.hr
Received: 24 March 2026. Accepted: 05 May 2026.
Available online: 26 October 2026

effects through electrokinetic coupling, without requiring empirical shape factors (**Glover et al., 2006; Rashid et al., 2015**). The RGPZ model has demonstrated greater predictive performance compared to Kozeny–Carman formulations in both clastic and carbonate rocks, particularly for tight carbonates where conventional models fail (**Rashid et al., 2015**). Recent machine learning studies on tight carbonate permeability prediction have confirmed that RGPZ outperforms conventional empirical models, providing the lowest prediction error (RMSE = 0.458) among physics-based approaches (**Al Khalifah et al., 2020**). The RGPZ approach operates at the continuum scale, capturing overall connectivity and tortuosity of the pore network without requiring explicit geometric characterization of individual pores and throats. Complementary to such continuum approaches, pore-scale methods directly resolve the geometry of individual flow paths, enabling incorporation of local throat constrictions, pore shape variations, and spatial heterogeneity into permeability calculations.

Geometric parameters that link pore morphology to hydraulic conductance play a central role in pore network models (PNMs). Among them, the hydraulic radius, $r_h = A/P$, is one of the most widely used because it combines information on pore size and wetted surface into a single length scale. In its classical single-conduit form, the hydraulic radius is defined as the ratio between cross-sectional area and wetted perimeter and is common in open-channel hydraulics and in pore-network representations where individual throats are replaced by equivalent simplified conduits (**Bernabé et al., 2010**). For internal flows in ducts and tube-like geometries, it is often convenient to express the same geometric information in terms of the **hydraulic diameter**, $D_h=4A/P = 4r_h$, which recovers the physical diameter for a circular pipe and is widely used in pipe-flow correlations and non-circular duct analogies (**Cai et al., 2014**).

Pore shapes in real porous media are far from regular and often non-convex, which further complicates their geometric representation and hydraulic characterization. In pore network modelling (PNM), such complex geometries are commonly approximated by idealized cross-sectional shapes such as circles, squares, triangles, ellipses, and three-corner star geometries. A widely used descriptor in that context is the shape factor, defined as $G = A/P^2$, where A is the cross-sectional area and P is the perimeter. For a circle, $G=1/4p$, is maximal, whereas any deviation from circularity lowers G, increases wet perimeter, and reduces hydraulic efficiency for a given area. However, it should be noted that for highly irregular pores, the effective hydraulic perimeter may be smaller than the measured optical perimeter due to the formation of stagnant zones and the positioning of the shearing plane. Shape-dependent hydraulic resistance has been analyzed in detail, demonstrating the strong influence of cross-sectional geometry on flow behaviour. Within generalized permeability formulations, such effects are often absorbed into geometric constants or dimensionless correction terms that account for pore shape, pore-radius heterogeneity, and coordination number (**Mortensen et al., 2005**). Based on G, irregular pore shapes can be mapped to canonical geometries, while complementary dimensionless quantities such as $H = r_h / r_{ins}$ relate hydraulic radius to inscribed radius and help compare hydraulic behaviour across different pore types (**Helland et al., 2008**).

Srisutthiyakorn & Mavko (2017) define an apparent radius as the geometric mean between a hydraulic radius and the radius of a circular pipe having the same porosity as the conduit under consideration. This construction reduces the bias of standard Kozeny–Carman-type descriptions when applied to non-circular and axially varying pipes and improves agreement with lattice Boltzmann simulations on sinusoidal pipes and sphere packs. The same geometric-mean concept underlies formulations in which area-derived and perimeter-derived radii are combined to balance sensitivity to flow cross-section and boundary complexity (**Srisutthiyakorn & Mavko, 2015**).

Modern PNMs extend these early concepts by employing a network of pores and throats with assigned local hydraulic conductances. In most PNMs, single-phase throat conductance is computed using Hagen–Poiseuille-type relations, which assume cylindrical or otherwise simple cross-sections so that conductance scales with radius to the fourth power or similar radius–shape relationships. This enables efficient simulation on large networks but requires mapping complex throat cross-sections into equivalent radii and shape factors - a step that becomes increasingly approximate as real pore geometry deviates from ideal assumptions (**Xiong et al., 2016**).

Extensions that incorporate shape factor, aspect ratio, specific surface, or fractal descriptions attempt to improve fidelity, but they still rely on simplifying assumptions about cross-sectional morphology and often require empirical closures (**Xiao et al., 2023**). A key strength of PNMs is the direct availability of geometric descriptors that can be statistically linked to permeability, including pore-size distributions, throat-radius distributions, coordination number, and tortuosity (**Ben-Noah et al., 2024**). However, conventional PNMs simplify geometry during extraction, reducing irregular pore bodies and axially varying throats to nodes and links with equivalent radii and shape factors, thereby subsuming geometric detail into empirical conductance corrections.

Furthermore, many PNM frameworks compute geometric characteristics based on idealized approximations rather than directly from real pore morphologies, which weakens the physical link between geometry and hydraulic conductance. The topological structure of the network is also influenced by segmentation thresholds and assumptions made during skeletonization or medial-axis extraction (**Thomson et al., 2018, Wang et al., 2019, Neumann et al., 2021**).

Many classical permeability and pore-network models express permeability in terms of bulk parameters while treating pore shape and topology only implicitly. Morphological studies have shown that parameters such as shape factor, pore-perimeter statistics, and fractal descriptors vary significantly at constant porosity and strongly influence permeability (**Graczyk et al., 2020**). Moreover, no widely adopted method simultaneously combines geometric fidelity, computational efficiency, and explicit representation of pore-scale morphology across both simple (artificial) and complex geometries. Pore network models (PNMs) are computationally efficient and straightforward to implement, but rely on simplified geometric representations and conductance models, whereas direct numerical simulations (DNS) provide higher-fidelity solutions at significantly greater computational cost.

Voxel-based DNS resolves the segmented pore space without geometric abstraction and can serve as a high-fidelity reference for permeability estimation. However, DNS typically does not provide explicit decomposition of permeability into interpretable geometric contributions and remains computationally demanding for large representative volumes (**Huang et al., 2020**).

Recent hybrid and multiscale workflows attempt to bridge this gap by combining network descriptions with voxel-resolved simulations and integrating experimental and imaging approaches (**Foroughi et al., 2025**). Nevertheless, a unified framework that preserves geometric realism while enabling structured and interpretable permeability estimation remains lacking.

Existing permeability estimation approaches either rely on simplified geometric abstractions, as in pore network models, or on computationally intensive direct numerical simulations, with limited capability to bridge geometric realism and computational efficiency. Furthermore, many models do not explicitly account for axial variability, pore connectivity evolution, or the dominant influence of flow-path constrictions. As a result, there remains a lack of a unified framework that can consistently describe permeability across both idealized geometries and complex pore networks while maintaining a direct and interpretable link to pore-scale geometry.

2. Methods and Materials

The main aim of this work is twofold. First, to do controlled testing on simplified geometries using tube-like models with prescribed roughness, axial variability, and connectivity thus quantify the impact of individual geometric factors on permeability. Second, transferring the insights gained from simple geometries which are further applied to heterogeneous rock samples, enabling interpretation of how resolution and morphological complexity influence effective permeability. In this chapter, an overview of the GMR method concept is given, followed by the development and the usage of artificial and real rock models.

2.1. Conceptual foundations of the GMR method

Permeability in heterogeneous porous media arises from the cumulative hydraulic resistance imposed by pore morphology, axial constrictions, and network connectivity across multiple length scales. The geometric mean radius (GMR) workflow is founded on the premise that these multiscale effects can be decomposed into hierarchical geometric contributions and reassembled into an effective permeability without explicitly solving the governing flow equations.

The central idea is to treat the segmented three-dimensional pore space as a sequence of geometrically resolved cross-sections orthogonal to a prescribed macroscopic flow direction. At each cross-section, connected pore regions are identified directly from the voxelized geometry and characterized by their measurable geometric properties (e.g. area, perimeter, centroid location). These quantities are used to derive an effective local hydraulic descriptor that reflects both pore size and shape complexity as well as solving the flow path trajectory.

The method operates on the premise that hydraulic conductance is fundamentally governed by local cross-sectional geometry and that macroscopic permeability results from serial and parallel integration of these local contributions along the principal flow direction.

The algorithm first finds the global connected volume by "flooding" technique, on desired flow axis, starting from both sides of the sample. This way, all isolated pores which do not contribute to the flow are eliminated. Next, the algorithm is searching pore by pore and slice by slice to track all the connections. For each pore in slice i, it searches for its parent pores in slice i-1 and its child pores in i+1 slice. All the connections are indexed and stored in the corresponding table. Additionally, all required geometrical properties are being calculated and added to the table. Prior to permeability calculations, all the pores in every slice have a pore, child and parent indexes, calculated geometrical properties (area, perimeter, hydraulic radius, GMR), as well as its individual pore permeability and area fractions squared, required for serial permeability calculations. When calculating serial permeability, additional correction is made to account for the tortuous flow paths. A tortuosity function (τ) is applied with the goal of defining the average flow path between the connected parent – child pores. The function operates as classical Euclidian distance calculations between the pores' centers of mass. The conceptual framework separates permeability estimation into three interacting levels:

(1) Local (Pore-Scale) Contribution

The three-dimensional pore space is represented as a binary voxel field and partitioned into planar cross-sections orthogonal to the macroscopic flow direction z. Within each slice, connected pore regions are identified and characterized using directly measurable geometric

quantities, pore area, perimeter and centroid position. At the pore scale, each connected pore region within a slice is assigned a local hydraulic conductance derived from its geometric properties, namely geometrical mean radius.

In this work, we define the geometric mean radius as:

$$r_{GM} = \sqrt{r_e r_h}, \quad (1)$$

where r_e is the equivalent circular radius, defined as:

$$r_e = \sqrt{\frac{A}{\pi}},$$

where A is the pore area. Hydraulic radius can be defined as:

$$r_h = \frac{A}{P}, \quad (2)$$

where A and P are pore area and perimeter respectively (**Wei et al., 2023**). In this work, a multiplier M is used as a scaling factor for switching between the regular (tube-like) geometries and heterogeneous porous media:

$$r_{hm} = M \times \frac{A}{P}, \quad (3)$$

Simple tube geometries favor $M = 2$ which translates original r_h to D_h, while micro-CT rock models are using $M = 1$ which is consistent with the actual r_h formulation.

The individual pore (local) permeability in this work is then obtained by:

$$k_i = \frac{r_{GM}^4 \pi}{8 A_s}, \quad (4)$$

where A_s is the total cross-sectional area of the slice.

Through GMR parameter, multiple conductance related features are reflected:

- Cross-sectional area.
- Pore boundary complexity (through perimeter).
- Shape irregularity.
- Local throat constriction.

This representation enables systematic testing of how roughness, resolution loss, or artificial geometric perturbations influence the effective pore-scale conductance in regular, simple geometries.

(2) Axial (Slice-Scale) Aggregation

Adjacent slices are linked through voxel overlap to identify pore continuation, splitting, and merging events. Hydraulic contributions are propagated along the principal flow direction using harmonic averaging analogies to obtain the conductivity of the touching pores in several (i) serial aggregations for axial continuation, (ii) area-squared weighted redistributions for splitting, and (iii) parallel aggregations for merging pores. This slice-wise propagation enables explicit quantification of constriction severity, axial variability, branching frequency, and tortuous path development.

Instead of constructing an idealized pore network, connectivity is determined directly from the voxel image, pores are linked only when their 3D pore regions touch or overlap in neighboring slices at each slice. In case of multiple connections, e.g. one parent pore and multiple children or a few child pores joining to a parent pore, different formulations are used. For splitting pores, squared area weighting is used to distribute parent pore conductance among its children. When it comes to merging of pores, all the contributing parent pores permeabilities are summed together.

(3) Network (Global) Integration

Global permeability is obtained through recursive aggregation of slice-level contributions. The resulting effective permeability can be expressed conceptually as $k = F(k_{pore}, k_{slice}, k_{network})$, or, equivalently, in geometric terms, as a function of morphology and topology (connectivity). **Figure 1** displays a schematic preview of the GMR pore shape approximations for pores in connecting slices, including the 3 types of connections: 1 to 1 connection, splitting and merging of the pores.

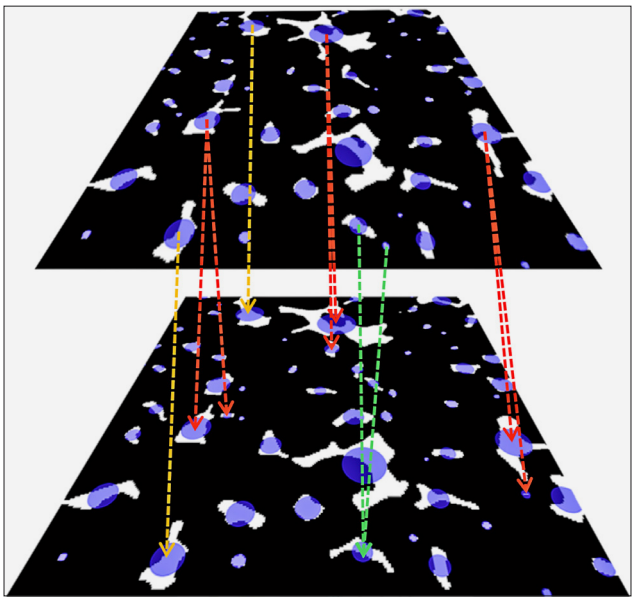
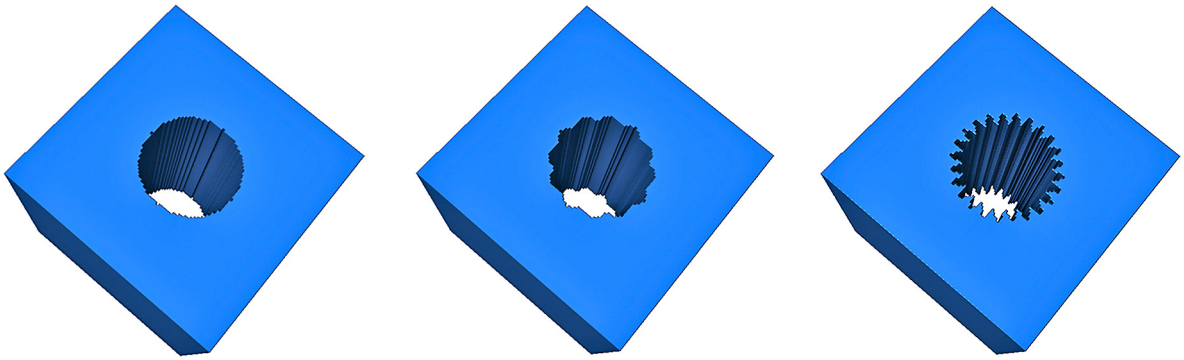


Figure 1: Schematic representation of Geometric Mean Radius (GMR) permeability approximations between connecting slices. White regions represent the actual pores resolved through micro-CT scanning and segmentation, while blue regions represent their corresponding GMR approximations. Regarding connectivity, orange lines indicate direct 1-to-1 pore connections, red lines denote pore splitting, and green lines represent merging cases.

2.2. Development and usage of testing geometries

The influence of various geometric features on permeability **was first investigated** through tests on a set of simple, synthetic pore geometries The GMR method was evaluated both at the pore scale (2D cross-sections) and at the full 3D scale. Tube like models with controlled



Smooth Wavy Rough

Figure 2: Representation of the 3 models used to observe the effect of pore roughness on the overall permeability

Table 1: Basic geometric properties of the used models for roughness testing

Tube type	Cross-section, µm²	Area, µm²	Perimeter, µm	G	r_e, µm	r_h, µm	GMR, µm
Smooth	10 000	1 257	132	0.072	20.003	19.062	19.527
Wavy	10 000	1 257	140	0.064	20.003	17.972	18.960
Rough	10 000	1 261	255	0.019	20.035	9.893	14.078

roughness, axial constrictions, and prescribed branching schemes were generated in *Python* programming language software. Using such regular geometries has two key advantages: their permeabilities can be obtained analytically or from well-defined reference solutions, and their simplicity allows us to isolate discretization effects and systematically compare GMR against different numerical solvers.

1) Models for testing roughness

Three distinctive models were created shown in **Figure 2**, to account for different levels of roughness. The first is the smoothest one representing a regular tube while the last one is the roughest, toothed tube. All 3 models are 100^3 voxels in volume where the tubes radius is approximately 20 µm. In GMR permeability calculations, used model resolution is set so that 1 px equals 1 micron. General features of each of the models used are given in **Table 1**.

2) Shape dependencies

Besides simple regular geometries, the GMR method was also applied to extruded tubes with varying cross-sectional shape complexity (see **Figure 3**). The individual pore shapes were sampled from the Imperial College London (ICL) micro-CT database, as reported by **Dong (2008)**, and then extruded along the flow direction to form tube like models. These realistic pore cross-sections isolate the influence of perimeter on hydraulic behaviour through roughness, boundary corrugation, and general deviations from circular geometry. In this context, the effect of shape can be quantified using a shape factor G where circular pores maximize G and therefore enclose the largest area for a given perimeter, while more irregular pores have lower G, larger wetted perimeters, and reduced hydraulic efficiency at fixed area. By testing GMR on these extruded pores, we explicitly probe how variations in shape factor and perimeter to area ratio translate into changes in the effective hydraulic radius and permeability predicted by the method. Geometric properties for each tube-like model are given in **Table 2**.

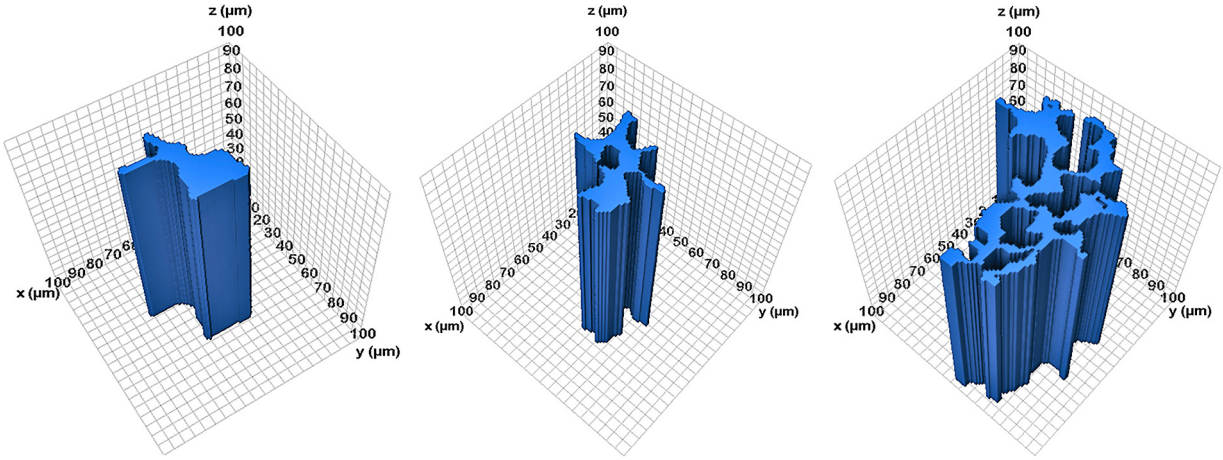
In comparison with the roughness models, these pores exhibit much lower values of the shape factor G. This could indicate that G alone does not fully capture pore roughness in a physically meaningful way. For the pores used in the shape analysis, the GMR approach does not significantly underestimate permeability. An illustrative example is provided by Pore stack-3, which has an approximately three times larger cross-sectional area than Pore stack-1, yet results in lower permeability. This clearly demonstrates the strong influence of pore shape on flow behaviour, beyond what is reflected by pore size alone.

3) Testing of the flow path constriction effect

The constricted tube model is designed to isolate the effect of axial flow path restrictions on permeability. It consists of three parallel flow channels that contain segments of larger diameter but also one or more narrow constrictions acting as critical pore throats (see **Figure 4**). In such a series arrangement, the effective permeability of each channel, and of the composite system, is largely controlled by the segment with the smallest diameter, while wider sections contribute comparatively little to the overall hydraulic resistance. Conversely, constrictions that are located away from the main high permeability trajectories have only a minor influence on the global permeability. The synthetic volume used for this test has a cross-sectional size of 300 × 300 voxels

Table 2: Basic geometric properties of the models used for shape inspection

Tube type	Cross-section, µm²	Area, µm²	Perimeter, µm	G	r_e, µm	r_h, µm	GMR, µm
Pore stack-1	10000	551	150	0.024	13.243	7.339	9.859
Pore stack-2	10000	533	218	0.011	13.025	4.889	7.980
Pore stack-3	10000	1469	659	0.003	21.624	4.460	9.820



Pore stack-1 Pore stack-2 Pore stack-3

Figure 3: Extruded pores of various shapes and complexity

Table 3: Theoretical geometrical properties of the created tubes for inspection of flow path restriction and HP calculations

Constricted tube 1		Constricted tube 2		Constricted tube 3	
Diameter, µm	Length, µm	Diameter, µm	Length, µm	Diameter, µm	Length, µm
4	30	50	40	50	20
40	20	4	30	20	50
50	50	30	30	4	30

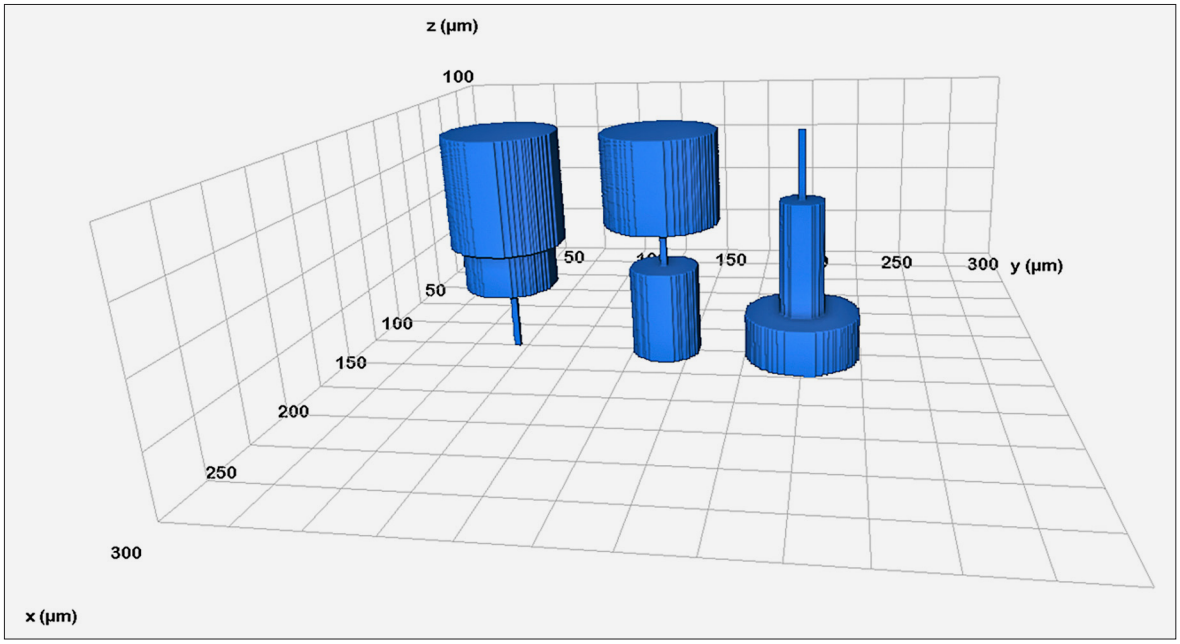


Figure 4: Visualization of the 3D model used for testing the effect of flow path constrictions

and a length of 100 voxels in the flow (z) direction, with an isotropic voxel size of 1 µm. The diameter and length of each tube segment, also used for analytical HP calculations, are provided in **Table 3**.

Table 4: Geometrical properties of the branching model

Pore area (μm²)	Perimeter (μm)	Equivalent circular radius (μm)	Hydraulic radius (μm)	GMR (μm	k_i (μm²)
437	92	11.79	9.50	10.59	0.2191
109	44	5.89	4.95	5.40	0.0149
25	20	2.82	2.50	2.66	0.0009

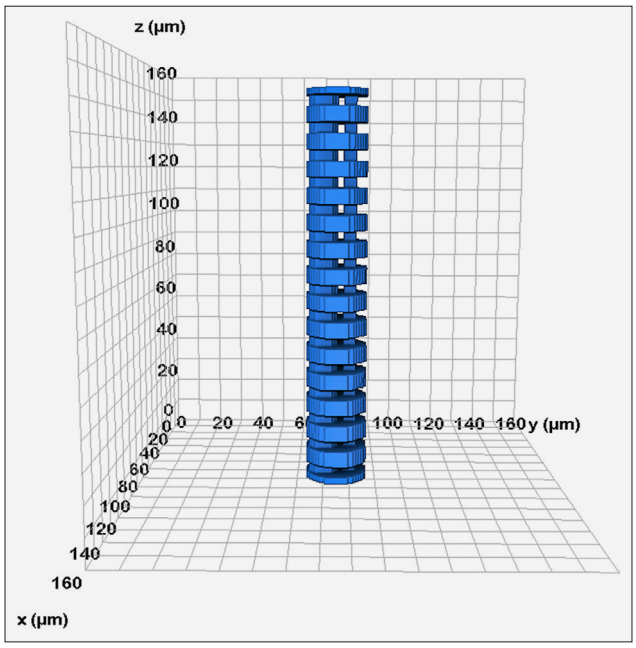


Figure 5: Preview of the branching model where repeating segments of pore splitting and merging occur

4) Pore network branching inspection

A simple model incorporates repeating splitting and joining segments, **Figure 5**. Basic geometric properties for each segment (pore) for the branching model are given in **Table 4**. At the beginning, the first 3 slices are occupied by a larger pore (437 μm²) at the top after which it splits to two smaller pores (109 and 25 μm²), which continue for the next 4 slices before merging again into the same larger pore. This 10-slice scheme is then repeated until the end of the model. The total size of the model is 150³ voxels large. The major goal of this model was to observe and test the splitting and merging schemes, i.e. area squared permeability weighting in the case of pore splitting and the plain summation in the case of merging pores.

5) Real rock samples

To further assess the GMR method on real rock samples and relate these results to those obtained on regular geometries, digital rock benchmarks from the Imperial College London (ICL) micro-CT database are used, originally introduced by **Dong (2008)**. The dataset comprises nine sandstone and two carbonate samples that have been already used in pore scale flow studies. Basic sample properties and Dong's LBM permeabilities for all samples are summarized in **Table 5**. These results serve as a permeability reference in this work. In addition, and in analogy to the regular geometry tests, we apply several other numerical methods (OpenLB, PerGeos LBM and Stokes solver) to these ICL volumes to span the range of available permeabilities and to relate differences between methods to the detailed geometric characterization of the pore space and its network connectivity.

Table 5: Properties of used ICL micro-CT rock volumes (**Dong, 2008**)

Sample	Resolution, (μm)	Size, voxel	Porosity, (%)	Permeability, (mD)
S1	8.638	300³	14.13	1 312
S2	4.956	300³	24.63	3 394
S3	9.100	300³	16.86	109
S4	8.960	300³	17.13	215
S5	3.997	300³	21.13	4 440
S6	5.100	300³	23.96	10 951
S7	4.803	300³	25.05	6 037
S8	4.892	300³	33.98	12 936
S9	3.400	300³	22.17	1 844
C1	2.857	400³	23.26	1 053
C2	5.345	400³	16.83	18

2.3. Different numerical methods used for permeability estimation

We employed several complementary numerical approaches in order to provide a robust reference for the GMR permeability estimates and to characterize pore space connectivity. OpenLB, an open-source Lattice Boltzmann (LBM) solver, was used to compute single phase permeability for both the synthetic tube geometries and the ICL digital rock samples. PerGeos' grid-based solver (GBS) was applied to the same segmented volumes as an alternative, enabling to assess sensitivity to discretization scheme and solver implementation. In addition, maximal ball pore network models, extracted in PerGeos, provided independent connectivity estimates by delivering coordination numbers and pore statistics which were compared directly to GMR derived connectivity metrics.

A key distinction among these approaches is that maximal ball PNM operates on a fully extracted 3D pore network, whereas GMR connectivity is evaluated at the pore/slice (2D) level based on voxel overlap between

neighboring slices. The PNM is therefore well suited for characterizing digitized rock samples but is not intended for the simple tube-like test geometries, for which direct voxel-based or analytical solutions are more appropriate. For the LBM and grid-based solvers, model size had to be constrained: very small domains led to undeveloped flow fields and unreliable permeability estimates, whereas very large domains were computationally prohibitive, a limitation that applied similarly to both OpenLB and the PerGeos grid-based solver. Taken together, these methods span the main classes of pore scale models—direct numerical simulation on voxels, continuum grid solvers, and extracted PNMs—and thus bracket the range of available permeability values for a given micro-CT volume.

3. Results and Discussion

The influence of pore scale geometry on global permeability is first examined using numerical simulations on regular and simplified model geometries. Attention is given to changes in pore perimeter and hydraulic radius, since the hydraulic radius $r_h = A/P$ explicitly contains the perimeter and therefore has a strong, direct impact on permeability estimates. Overestimation of the perimeter reduces r_h and leads to underestimation of permeability, whereas underestimation of the perimeter has the opposite effect. To mitigate irregularities arising from complex pore shapes, the GMR formulation uses a geometric mean radius that balances pore geometry and hydraulic efficiency.

In this study, in addition to the classical hydraulic radius expression, a modified hydraulic radius is introduced via a scaling factor M, which acts as a resistance controller. Its use reflects the observation that pore geometry and hydraulic performance do not follow a single universal relationship across the spectrum from ideal capillary tubes to complex natural pore networks. Since r_h is related to the pore perimeter, in this work two different perimeter types (PTs) are used. Generally, weighted boundary length (Python's scikit-image *skimage.measure* function) perimeter type 1 (PT1) is preferred for both simple geometries and real rock models, because it mitigates the staircase effect of voxelized boundaries compared to a simple pixel count perimeter. On the other hand, results obtained using PT0 (pixel counting) are given to show the magnitude of perimeter effect on the permeability.

- **Idealized and Capillary Regimes ($M = 2$)**

A value $M=2$ is applied for regular, tube-like geometries in which a fully developed parabolic velocity profile is expected. In this regime, the scaling performs a geometric restoration of the hydraulic radius toward the characteristic dimension of an equivalent cylindrical conduit. Even for mildly irregular shapes where the wetted perimeter exceeds that of a circle, this choice of M increases the effective hydraulic radius so that the predicted conductance approaches the theoretical upper limit defined by the pore cross-sectional area (*via* the equivalent radius r_e). This scaling is therefore consistent with high efficiency flow regimes in which wall drag is relatively weak despite small deviations from circularity.

- **Complex and High-Conductance Porosity ($M = 1$)**

Real-world pore networks, identified via 3D micro-CT imaging, often exhibit high irregularity. While small, poorly connected pores may approach an ideal Shape Factor ($G=1/4p$), they minimally contribute to overall permeability. Conversely, primary flow-pathways typically exhibit low G values due to convoluted shapes and wall rugosity. Simultaneously, the scaling exponent M is reduced toward unity to account for increased flow resistance and the reduction of effective hydraulic efficiency caused by the expanded wetted perimeter and wall rugosity inherent in irregular pore shapes.

Within the GMR formulation, an entire pore cross-section is assumed to participate in flow, mirroring the situation in simple tube geometries where the cross-sectional area does not change along the axis. This simplification can be reasonable for homogeneous, high-resolution models or for relatively simple networks, but in more realistic rock samples the full cross-section may not be equally involved in transport: overlapping areas between connected pores can be limited, and flow may be concentrated in subregions of the pore cross-section, especially near constrictions and branching points. As a result, a dependence of GMR based permeability on image resolution is expected.

3.1. Permeability results for simple geometries

Simple geometrical models introduced in the previous section are used alongside real rock samples to analyze permeability behaviour. The simple models provide controlled test cases in which individual geometric effects roughness, shape, constrictions, and branching can be isolated, while the rock samples represent more realistic pore networks with all the effects combined. Results from these models are used to examine both the spread in permeability predicted by different numerical methods and the role of the GMR scaling factor M as a function of pore morphology and connectivity. The subsequent sections then present GMR permeabilities for the micro-CT rock samples together with their geometric characterization, with the aim of delineating the conditions under which the GMR method is most reliable and outlining practical constraints on its applicability.

3.1.1. Pore roughness

Three tube-like models with identical nominal radius but different wall morphology (smooth, wavy and rough) are considered in order to quantify the impact of pore roughness on permeability (see **Figure 2**). **Table 6** re-

Table 6: Permeability results for testing the impact of pore roughness

Model type	GMR, *M*=1 mD	GMR, *M*=2 mD	PG-GBS mD	PG-LBM mD	OLB mD
Smooth	1 446	5 785	4 432	6 241	5 516
Wavy	1 286	5 142	4 261	5 949	5 285
Rough	391	1 563	3 554	4 465	3 885

Table 7: Results obtained for pore shape analysis

Model name	Perimeter type	*M*	*τ*	GMR mD	PG-LBM mD	PG-GBS mD	OLB mD
Pore-1 stack	1	2	FALSE	377	552	597	497
Pore-2 stack	1	2	FALSE	161	192	248	172
Pore-3 stack	1	2	FALSE	370	424	494	375

ports the resulting permeabilities for all numerical methods and for two choices of the GMR scaling factor. When *M = 2*, GMR permeabilities for the Smooth and Wavy models agree well with OpenLB, while PerGeos GBS values *M* are slightly lower; for the rough model, however, GMR significantly underestimates permeability compared to all other methods. Using *M=1*, which is adopted for real porous media in this work, leads to a systematic underestimation for all three roughness levels. The analytically computed permeability for the Smooth case, obtained from the Hagen–Poiseuille/Darcy relation on the ideal continuous geometry, is 6366 mD. Among the numerical methods, PerGeos LBM most closely reproduces this reference, reflecting the absence of pixelization effects in the analytical solution. It should be emphasized the rough geometry represents exaggerated roughness, more extreme than is typically observed in most rock pore networks. As such, they serve primarily to delineate the sensitivity limits of the GMR method to perimeter inflation: at fixed radius, increasing roughness suppresses permeability, and GMR responds by strongly reducing the effective hydraulic radius once the perimeter becomes large.

3.1.2. Pore shape effect

For the so-called capillary geometries, the effect of pore shape complexity is examined using extruded pore cross-sections ("pore stacks") with different morphologies but identical topology and constant cross-section along the flow direction. **Table 7** summarizes the permeability results for these three pore stack models. As in the roughness tests, these are tube-like systems without changes in connectivity, coordination number, or axial constrictions, so any differences in permeability arise solely from cross-sectional shape. In this case, PerGeos GBS permeabilities are consistently higher than both OpenLB and GMR values, whereas GMR yields the

Table 8: Results for constriction model testing where GMR results are using *M* =2

Permeability method	Permeability, mD
Analytical (Hagen-Poiseuille)	0.707
PG	0.884
OLB	0.533
GMR	0.747

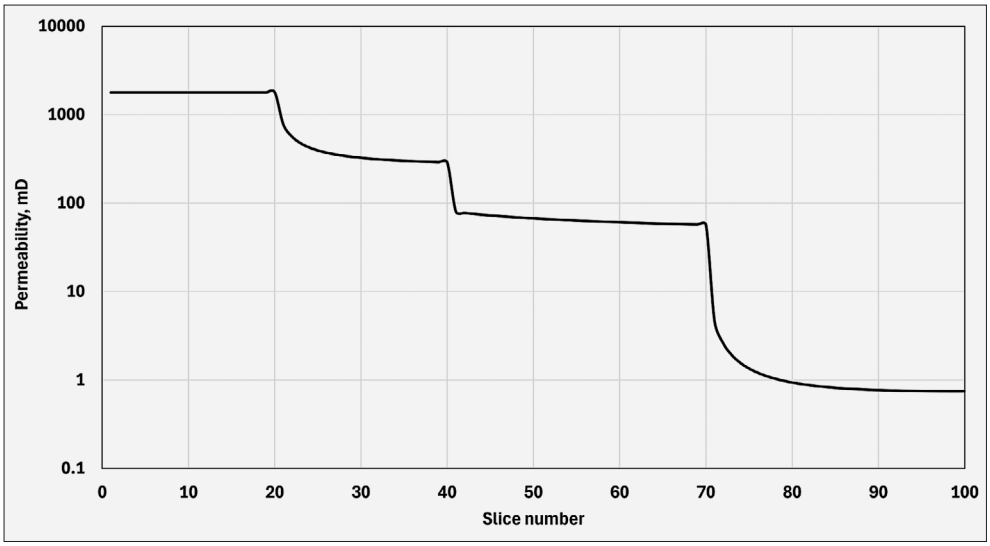


Figure 6: Cumulative permeability distribution with respect to the slice number in the z direction, over 100 slices

Table 9: Results obtained for testing of the pore network branching model

Perimeter type	*M*	*τ*	GMR *k*, mD	PG LBM *k*, mD	PG GBS *k*, mD	OLB *k*, mD
0	1	TRUE	6.2	29.1	33.5	24.2
0	1	FALSE	9.0	29.1	33.5	24.2
0	2	TRUE	24.6	29.1	33.5	24.2
0	2	FALSE	36.0	29.1	33.5	24.2
1	1	TRUE	9.6	29.1	33.5	24.2
1	1	FALSE	14.0	29.1	33.5	24.2
1	2	TRUE	38.2	29.1	33.5	24.2
1	2	FALSE	55.8	29.1	33.5	24.2

Table 10: Results for different numerical methods using repeating geometry model

Model thickness (Nz)	Perimeter type	*M*	*τ*	GMR *k*, mD	PG LBM *k*, mD	PG GBS *k*, mD	OLB *k*, mD
100	2	2	TRUE	38.2	29.1	33.5	24.2
150	2	2	TRUE	38.2	29.1	33.9	24.2
200	2	2	TRUE	38.2	29.1	34.1	24.2

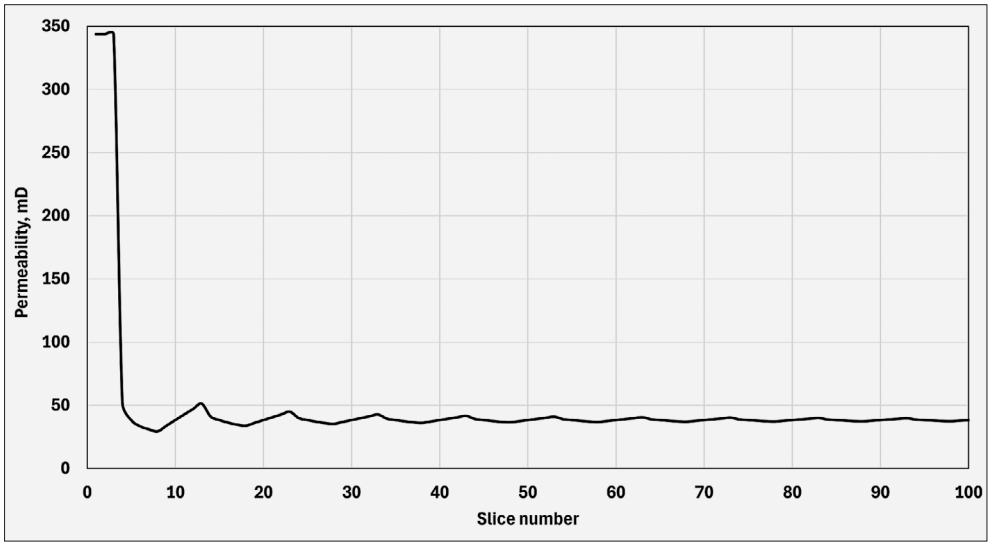


Figure 7: Permeability evolution and stabilization for the branching tubes model

lowest permeabilities for all three shapes. Nevertheless, for Pore 2 and Pore 3, GMR permeabilities are close to OpenLB, indicating that in pure pore stack configurations (no topology change) the GMR method behaves as a more conservative estimator for simpler shapes, while still tracking the LBM trend for the complex ones.

3.1.3. Flow path restrictions

The impact of axial flow path restrictions is examined using the constricted tubes model, with permeability results summarized in **Table 8** for both analytical and numerical approaches. Each of the three channels contains at least one narrow segment ("throat") of much smaller diameter than the adjacent sections, so that the overall permeability of the channel, and of the composite system, is dominated by these narrowest elements while the wider segments contribute comparatively little to the total hydraulic resistance. This behaviour is clearly visible in **Figure 6**, where sharp drops in cumulative permeability coincide with the axial positions of the constrictions.

For this model, no tortuous paths are detected by the GMR calculations ($\tau = 1$), and the PT 1 is used along with $M=2$. Under these settings, the GMR permeability for the constricted tubes model matches the analytical Hagen–Poiseuille solution more closely than the OpenLB result and lies between the PG GBS and PG LBM values, thereby confirming that the GMR series/parallel propagation logic correctly captures the dominant role of narrow throats in series.

3.1.4. Pore network branching

Natural pore systems are characterized not only by complex pore shapes but also due to changes in topology and connectivity, especially in more permeable rocks where highly branched networks offer multiple low resistance flow paths and allow fluids to bypass local con-

strictions. To investigate how the GMR framework handles splitting and merging of pores, a simple branching model is considered in which a large pore repeatedly divides into two smaller pores and then recombines further downstream (see **Figure 5**). According to the Hagen–Poiseuille scaling $Q \gg A^2$, flux (and thus permeability contribution) is expected to be strongly weighted toward the larger child pore when a parent pore splits, so the GMR implementation distributes conductivity among child pores in proportion to the squared pore area.

Since branching involves changes in flow direction, the model is evaluated with and without a geometric tortuosity correction. **Table 9** summarizes the main results for the perimeter and *M* values used. In contrast to the roughness and shape tests, using *M=2* does not lead to underestimation of permeability in this branching geometry. Instead, *M=2* combined with tortuosity correction and PT1 yields a GMR permeability value, which agrees best with OpenLB and PerGeos results while overestimating them. The results for this case are given in **Figure 7** where it can be observed how permeability stabilizes and fluctuates less with increasing model size. For comparison, Perimeter type 0 produces substantially lower permeabilities when tortuosity is included, particularly for *M=1*, reflecting the strong penalization of hydraulic radius caused by the shorter perimeter estimate. Interestingly, tests across several samples indicate that PT0 without tortuosity correction gives similar permeabilities to PT1 with tortuosity correction, suggesting a partial compensation between perimeter underestimation and increased path length.

Table 10 demonstrates that repeating the same branching segment multiple times does not change the converged permeability for any of the numerical methods, confirming that the chosen convergence criteria—especially for the grid-based Stokes solver—are appropriate for this type of network. Compared to the roughness, shape and constriction tests where GMR tended to underestimate permeability due to strong penalization of the hydraulic radius, the branching model shows the opposite tendency: when entire cross-sections are assumed to participate in flow, the simplified treatment of interfacial areas between merging and splitting pores leads to a less severe penalization, and GMR moves closer to or slightly above the other numerical estimates. Tortuosity plays a clear role in this behaviour. In the GMR framework, geometric tortuosity is computed as the mean ratio between the parent–child center of mass distance and the nominal slice spacing, with typical values between 1 and 2 (often around 1.5 for real rock samples). Using PT1 with *M=2* and applying this tortuosity correction reduces the initially overestimated permeability to values that more closely match LBM and GBS results, underscoring the importance of including tortuosity explicitly when branching and directional changes are significant.

3.2. Micro-CT rock samples

Actual micro-CT samples were used in order to test the applicability of GMR method in more real circumstances. Samples are part of Imperial College of London (ICL) database, given by **Dong (2008)**. The whole dataset consists of a total of 9 sandstone and 2 carbonate rock samples. The aim was to test the overall impact of joined effects like roughness, shape, resolution and network branching on the permeability and consequently, the scaling factor *M* required to match benchmarking methods.

The GMR method permeability for ICL samples presented in **Table 11** was obtained using PT1 with tortuosity correction as well as *M=1*. This setting provided good setup for comparing the results to other numerical methods. In **Table 14** values for required *M* factors are given, where the largest *M* is required to match PG-LBM and PG-GBS permeabilities. The results present hypothetical M values that would be required to force GMR predictions to match each reference method. It is important to note that M is not used as a tuning parameter in practice - the GMR method applies *M=1* to all rock samples without individual adjustment. This analysis serves as a diagnostic tool to identify outliers and samples where GMR's geometric assumptions break down.

The OLB and Dong-LBM results are generally in a good agreement with GMR values. It can also be seen that the largest discrepancy is obtained for S4 sample. The S4 mismatch can be interpreted as a joint effect of coarse resolution and simplifying assumptions in the GMR treatment of pore overlaps. At coarser voxel sizes, the evolution of pore shape and size from slice to slice is more abrupt than in fine resolution images, and the overlap between connected pores often becomes marginal rather than involving the full cross-section. In such cases, small overlapping regions act as critical throats for maintaining connectivity and controlling conductance. Since the current GMR implementation does not explicitly measure overlap area when computing series permeability but instead, use weights by parent and child pore areas, smaller pores can get penalized. In tight networks, where main channels terminate in severely constricted regions, this leads to a strong underestimation of total permeability. When main flow paths are well resolved and supported by multiple voxels, underestimation of some small pores or constrictions is less problematic because the dominant carriers of flow remain accurately represented. In low permeability, poorly resolved samples, however, these constrictions can control the entire network response. This suggests that tight rocks with low porosity and permeability require finer imaging resolution to capture the branching structure and throat geometry with sufficient fidelity for GMR and voxel-based DNS to perform reliably. A comparison of the permeability obtained by the different numerical methods and the reference data provided by **Dong (2008)** is presented in **Figure 8**.

Table 11: Permeability results obtained using ICL samples for different numerical methods

Sample	Resolution (microns)	Dong LBM (2008), mD	OLB, mD	PG-LBM, mD	PG-GBS, mD	GMR, mD
S1	8.638	1 312	1 531	2 063	2 427	444
S2	4.956	3 394	2 791	4 429	4 924	3 982
S3	9.1	109	85	787	1 365	79
S4	8.96	215	87	465	1 024	1
S5	3.997	4 440	4 765	6 183	6703	4 205
S6	5.1	10 951	9 679	13 318	13 485	12 554
S7	4.803	6 037	5 459	7 701	8 398	6 414
S8	4.892	12 936	11 862	15 570	16 153	11 777
S9	3.4	1 844	1 719	2 445	2 844	1 849
C1	2.857	1 053	854	1 354	1 511	1 023
C2	5.345	18	144	163	317	28

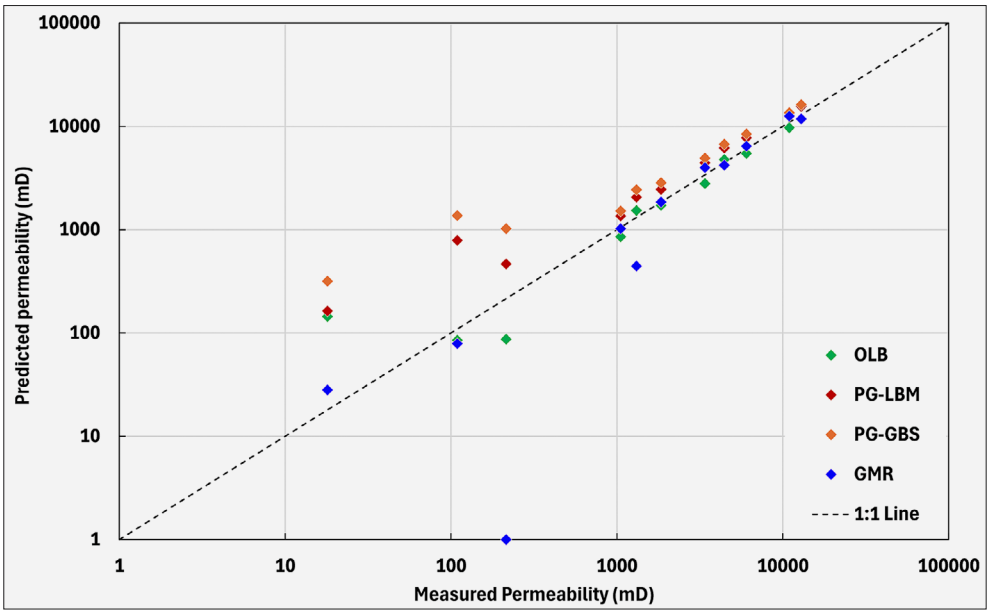


Figure 8: Cross-plot of reference (**Dong, 2008**) versus predicted permeabilities for ICL samples, obtained using OpenLB, PerGeos LBM, PerGeos GBS and GMR methods. The dashed line represents 1:1 agreement.

Despite these limitations, the distributions of M in **Table 14** indicate that, for most samples and for Dong LBM and OpenLB in particular, the median M is close to unity. PerGeos LBM and Stokes solver require slightly higher values but remain significantly below 2, in contrast to the idealized tube tests. At the same time, the overall numerical permeabilities results for the ICL samples are quite heterogeneous, and for several rocks it is difficult to identify a uniquely "correct" benchmark reference. Different LBM and grid-based implementations can differ by more than an order of magnitude, especially in tight, complex carbonates. This makes it impractical to designate any single numerical method as a definitive benchmark for calibrating GMR across the entire dataset. In practice, laboratory measurements would provide the most robust reference for real rocks when available, whereas for purely synthetic geometries such experimental constraints are not accessible.

Applications to micro-CT rocks from the ICL database reveal a clear distinction between regimes where GMR is predictive and regimes where both GMR and voxel-based DNS become strongly resolution dependent. For higher permeability, well connected sandstones and carbonates imaged at fine voxel size, GMR with M values close to unity reproduces permeabilities by other methods comparable to the spread among the other numerical methods themselves. In these samples, coordination numbers are high, pore throats are resolved by multiple voxels, and overlapping areas between connected pores are substantial, so the slice wise area weighting and perimeter based hydraulic radii provide a faithful representation of the main flow paths. Conversely, for low permeability samples with coarser resolution and pronounced constrictions, such as e.g. S3, S4 or C2, the numerical methods themselves disagree by more than an order of magnitude. These cases underline that the accuracy of any geometry-based model, including GMR, is ultimately bounded by the resolving power of the imaging and by how different solvers treat near voxel scale throats.

Taken together, the synthetic and micro CT results suggest that the GMR method is most appropriate for volumes where (i) pore throats are resolved in fine resolution and pore network evolution is slow, (ii) the pore network is moderately to highly connected, and (iii) main flow paths are not dominated by a few sub voxel constrictions on the main flow paths. In this regime, GMR offers a fast alternative to full DNS while retaining a clear geometric interpretation through its dependence on area, perimeter, and connectivity statistics. At the same time, the method shares with pore network approach a sensitivity to segmentation choices and image resolution in tight, rugose pore spaces. The results therefore support a pragmatic view in which GMR complements LBM and PNM: it can be used to screen large numbers of volumes, to decompose permeability into geometric contributions, and to benchmark against DNS in well resolved samples, while acknowledging larger uncertainty in very tight, poorly resolved rocks.

To quantitatively assess the accuracy of the GMR method and compare it against established numerical approaches, root mean square error (RMSE) analysis was performed across all ICL digital rock samples. RMSE provides a standardized metric for evaluating prediction quality by quantifying the average magnitude of deviation between predicted and reference permeabilities:

$$\mathrm{RMSE} = \sqrt{\frac{1}{n}\sum_{i=1}^{n}(\mathrm{Predicted}_i - \mathrm{Reference}_i)^2} \qquad (5)$$

where lower RMSE values indicate better agreement. To enable meaningful comparison across the wide permeability range in the dataset (18 mD to 12 936 mD), relative RMSE is also calculated and is defined as:

$$\text{Relative RMSE (\%)} = \frac{\mathrm{RMSE}}{\text{Mean of Reference Values}} \times 100 \qquad (6)$$

Relative RMSE normalizes the absolute error by the mean permeability magnitude, allowing direct comparison of prediction quality between high- and low-permeability samples.

The analysis results given in **Table 12** illustrate the agreement of four numerical methods (OpenLB, PerGeos LBM, PerGeos GBS, and GMR) against the **Dong (2008)** LBM permeability values. It should be noted that **Dong (2008)** LBM data are not considered ground truth but rather a logical reference choice, as the ICL samples were originally characterized by **Dong (2008)** and have been widely adopted as benchmarks in digital rock studies. In the absence of experimental core flooding measurements for these digital samples, all numerical methods represent approximations with inherent uncertainties, and no single solver can be deemed definitively "correct."

The results are divided by permeability range to assess method performance across different permeability magnitudes. OpenLB demonstrates the best overall agreement with reference values (RMSE = 580.8 mD, 15.1%), particularly in high-permeability samples (RMSE = 678.0 mD, 12.9%). GMR ranks second overall (RMSE = 691.3 mD, 18.0%), showing comparable performance to OpenLB in the high-permeability range (RMSE = 807.0 mD, 15.4%). Both PerGeos methods systematically predicted higher permeability, with PG-LBM and PG-GBS exhibiting relative RMSE values of 35.9% and 46.1%, respectively.

All methods show substantial disagreement for low-permeability samples (<1000 mD, n=3), where relative RMSE increases dramatically: OpenLB (91.8%), GMR (109.6%), PG-LBM (373.3%), and PG-GBS (771.6%). This universal deterioration reflects fundamental limitations of all the methods used when dealing with less de-

Table 12: Performance of all numerical methods with respect to **Dong (2008)** LBM results for each sample group

Category	Sample Group	RMSE (mD)	Relative RMSE (%)
All samples (n=11)	OLB	580.8	15.1
All samples (n=11)	PG_LBM	1381.0	35.9
All samples (n=11)	PG_GBS	1773.1	46.1
All samples (n=11)	GMR	691.3	18.0
≥1000 mD (n=8)	OLB	678.0	12.9
≥1000 mD (n=8)	PG_LBM	1598.2	30.5
≥1000 mD (n=8)	PG_GBS	2008.1	38.3
≥1000 mD (n=8)	GMR	807.0	15.4
<1000 mD (n=3)	OLB	104.6	91.8
<1000 mD (n=3)	PG_LBM	425.5	373.3
<1000 mD (n=3)	PG_GBS	879.7	771.6
<1000 mD (n=3)	GMR	124.9	109.6

Table 13: Root mean square error (RMSE) between GMR predictions and four reference permeability estimation methods across different sample groups

Reference Method	Sample Group	RMSE (mD)	Relative RMSE (%)
Dong_LBM	All samples (n=11)	691.3	18.0
Dong_LBM	≥1000 mD (n=8)	807.0	15.4
Dong_LBM	<1000 mD (n=3)	124.9	109.6
OLB	All samples (n=11)	1051.6	29.7
OLB	≥1000 mD (n=8)	1232.1	25.5
OLB	<1000 mD (n=3)	83.4	79.2
PG_LBM	All samples (n=11)	1494.2	30.2
PG_LBM	≥1000 mD (n=8)	1725.7	26.0
PG_LBM	<1000 mD (n=3)	494.9	104.9
PG_GBS	All samples (n=11)	1883.5	35.0
PG_GBS	≥1000 mD (n=8)	2128.4	30.2
PG_GBS	<1000 mD (n=3)	963.3	106.8

Table 14: Values for scaling factor *M* required to match benchmarking permeabilities

Sample	Dong LBM (2008)	OLB	PG-LBM	PG-GBS
S1	1.72	1.86	2.16	2.34
S2	0.92	0.84	1.05	1.11
S3	1.17	1.04	3.16	4.16
S4	12.83	8.16	18.86	27.99
S5	1.03	1.06	1.55	1.62
S6	0.93	0.88	1.03	1.04
S7	0.97	0.92	1.10	1.14
S8	1.05	1.00	1.15	1.17
S9	1.00	0.96	1.15	1.24
C1	1.01	0.91	1.15	1.22
C2	0.80	2.27	2.41	3.36
Average	**2.13**	**1.81**	**3.16**	**4.22**
Median	**1.01**	**1.00**	**1.15**	**1.24**

veloped pore networks and in resolving pore throat constrictions at the given imaging resolutions.

Further analysis was conducted, presented in **Table 13**, to comprehensively assess GMR agreement against all four numerical methods: **Dong (2008)** LBM simulations, OpenLB LBM, PerGeos LBM, and PerGeos GBS. This multi-reference comparison reveals method-specific biases and validates GMR performance against both literature benchmarks and contemporary numerical solvers. GMR shows strongest agreement with the **Dong (2008)** results for the complete dataset (18.0% relative RMSE) and high-permeability samples (15.4% for ≥1000 mD). However, for low-permeability samples (<1000 mD), GMR exhibits best agreement with OpenLB (79.2% relative RMSE), compared to Dong LBM (109.6%), PG-LBM (104.9%), and PG-GBS (106.8%).

The divergence between GMR and PerGeos methods (PG-LBM: 30.2%, PG-GBS: 35.0% for all samples) reflects fundamental methodological differences: PerGeos solvers consistently predict higher permeabilities than GMR across all samples, whereas GMR tends toward conservative (lower) estimates that align more closely with Dong's original simulations and OpenLB results.

The consistency of GMR performance across different reference methods, maintaining 15-26% relative RMSE for high-permeability samples regardless of reference choice, demonstrates that GMR predictions are method-independent and physics-based rather than empirically calibrated to match any single solver. The pattern of agreement indicates that GMR captures similar pore-scale flow physics to direct lattice Boltzmann implementations for well-connected, high-permeability samples, despite using a fundamentally different geometric-based approach rather than explicit flow simulation.

3.3. Geometric characterization

An additional characterization of the ICL samples was performed to clarify further the results and relate the key geometric parameters required for generating pore network models (PNM). The objective was to establish a relationship between the pore network geometry and permeability. An attempt was made to relate the shape factor *G* to the geometric and hydraulic characteristics of the pore space.

For all ICL samples, basic geometric descriptors are computed and their average values reported in **Table 15**. When the shape factor *G* is averaged uniformly over all pores, the resulting values are relatively high and often suggest nearly circular cross-sections. By contrast, when *G* is weighted by pore area, the mean drops sharply and no longer indicates circular geometry. This reflects the fact that many small pores are relatively regular and contribute strongly to the unweighted statistics, whereas the larger pores that dominate fluid transport tend to be more irregular, with low *G* and larger perimeters. The cumulative distribution of *G* versus pore area makes this distinction clear: regular, high *G* pores are numerous but small, while the largest pores that carry most of the flow lie in the low *G* tail. Plotting cumulative *G* against permeability for S8 sample (see **Figure 10**), shows a consistent trend in which permeability decreases as the dominant pore shapes become more regular (higher *G*), confirming that flow is preferentially organized in irregular, rough pores rather than in small, nearly circular ones.

When plotting the relationship between weighted *G* and permeability for all samples in **Figure 9**, a similarly indicative distribution is obtained. In general, permeability decreases as pore shapes become more regular, i.e. as they approach circular geometry. However, pore shape is not the only factor influencing permeability. The number of interconnections between pores also plays an important role. Therefore, a coordination number (CN) analysis was performed for each sample (see **Table 16**) and compared with the results obtained using the maximal ball (MB) method implemented in PerGeos. Examination of the data in **Tables 15** and **16** shows that there is little correlation between G, weighted G, M and CN, except for a weak functionality between *CN* and the weighted G. This lack of strong correlation underscores that permeability control in heterogeneous rocks arises from the coupled interplay of multiple geometric factors rather than from any single descriptor.

Since permeability also strongly depends on the coordination number, an additional analysis and comparison between the GMR and MB methods was performed. For some ICL samples, such as S3, S4 or S8, both methods yield more similar *CN* values. However, when considering all samples, no clear correlation is observed. Sample S8, for example, exhibits a very high *CN* for both methods. **Figures 11** and **12** display GMR derived coordina-

Table 15: Results for geometrical characterization of ICL samples

Sample	S1	S2	S3	S4	S5	S6	S7	S8	S9	C1	C2
Pore area, μm^2	14 462	8 514	5 509	4 976	12 258	24 154	14 720	21 090	6 949	2 919	4 072
Pore perimeter, μm	511	479	299	275	509	724	641	824	365	201	225
G	0.06	0.05	0.07	0.07	0.05	0.05	0.05	0.05	0.05	0.06	0.07
Weighted G	0.032	0.018	0.037	0.042	0.019	0.016	0.014	0.010	0.025	0.020	0.030
M	1.72	0.92	1.17	14.66	1.03	0.93	0.97	1.05	1.00	1.01	0.80
CN (GMR)	2.18	2.78	2.49	2.29	2.33	2.62	2.83	3.76	2.13	3.03	2.64

Table 16: Coordination number comparison between GMR and MB PNM methods

	Coordination number		Pore count	
Sample	GMR	MB	GMR	MB
S1	2.18	2.79	18 482	2 245
S2	2.78	4.06	18 773	3 123
S3	2.49	2.78	63 553	10 209
S4	2.29	2.30	65 675	11 059
S5	2.33	2.90	6 823	1 167
S6	2.62	4.04	6 669	1 499
S7	2.83	4.43	10 464	1 782
S8	3.76	4.08	9 003	3 380
S9	2.13	3.16	9 407	907
C1	3.03	2.81	24 810	10 013
C2	2.64	2.00	38 534	15 310

tion numbers for S8 and S4 samples respectively. Both slice average and cumulative *CN* values with respect to cumulative permeability are given. This information can be used to observe the evolution of the pore network and its degree of heterogeneity. Nevertheless, an important difference lies in the way pores are defined within each method and in the resulting pore count. The GMR approach does not distinguish between pores and throats; instead, in each slice all voxels not belonging to the solid phase are treated as part of the pore space. Consequently, the average *CN* obtained using the GMR approach is generally lower than that obtained with the MB method. However, given the significantly larger number of identified pores, the total number of connections is not necessarily smaller.

The geometric characterization of the ICL samples confirms that permeability is controlled by a coupled evolution of pore size, shape, and connectivity rather than by any single descriptor alone. Across the suite, higher permeability rocks systematically exhibit larger mean pore sizes, higher coordination numbers, and lower weighted shape factors, indicating that flow is preferentially organized in irregular but well-connected pathways rather than in small, nearly circular pores. In contrast, the tightest samples combine small characteristic pore sizes with low coordination numbers and relatively high weighted shape factors, consistent with a network dominated by short constrictions and isolated pores that contribute little to global transport.

From the perspective of the GMR method, these geometric trends help to explain why a single scaling factor *M* performs well over a broad range of sandstones and moderately tight carbonates but fails to fully correct more extreme cases. In well-connected samples with high conductance, weighted coordination and low weighted shape factor, the slice wise aggregation scheme and the geometric mean radius capture the dominant flow channels, and only modest adjustments of *M* are needed to match DNS permeabilities. In tight, low *CN* samples with many small, high *G* throats and limited

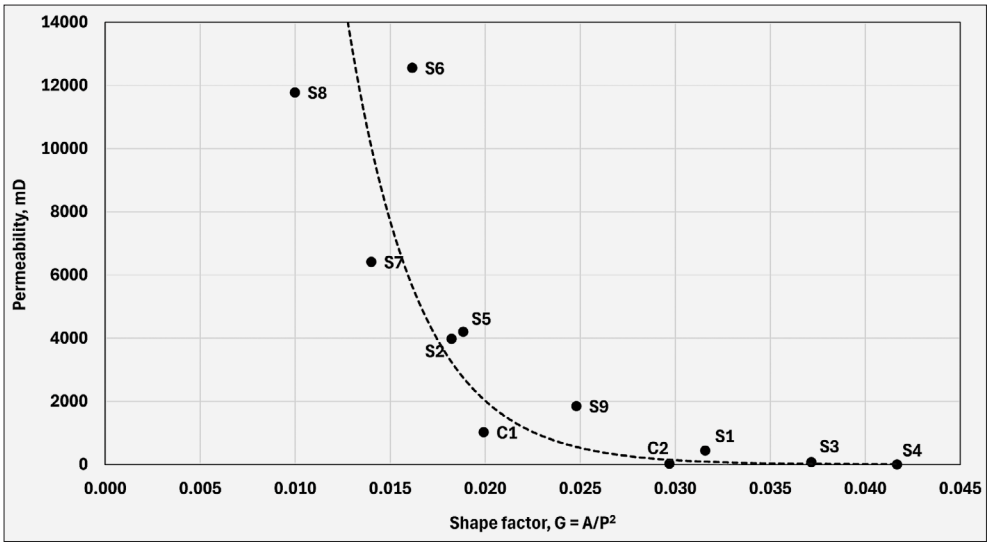


Figure 9: Correlation of weighted pore shape factor, *G* and respective permeability values

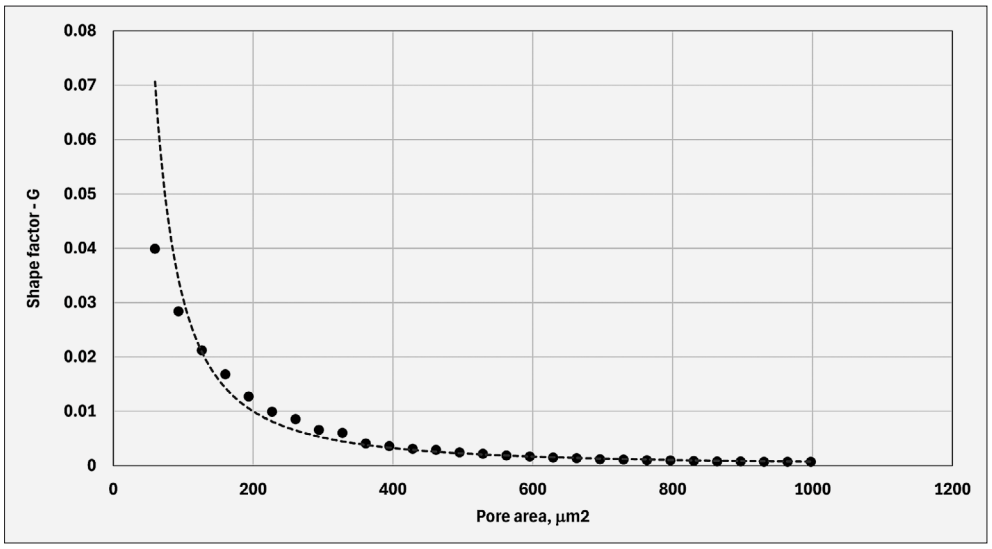


Figure 10: Correlation of pore shape factor *G* and respective permeability values for S8 sample

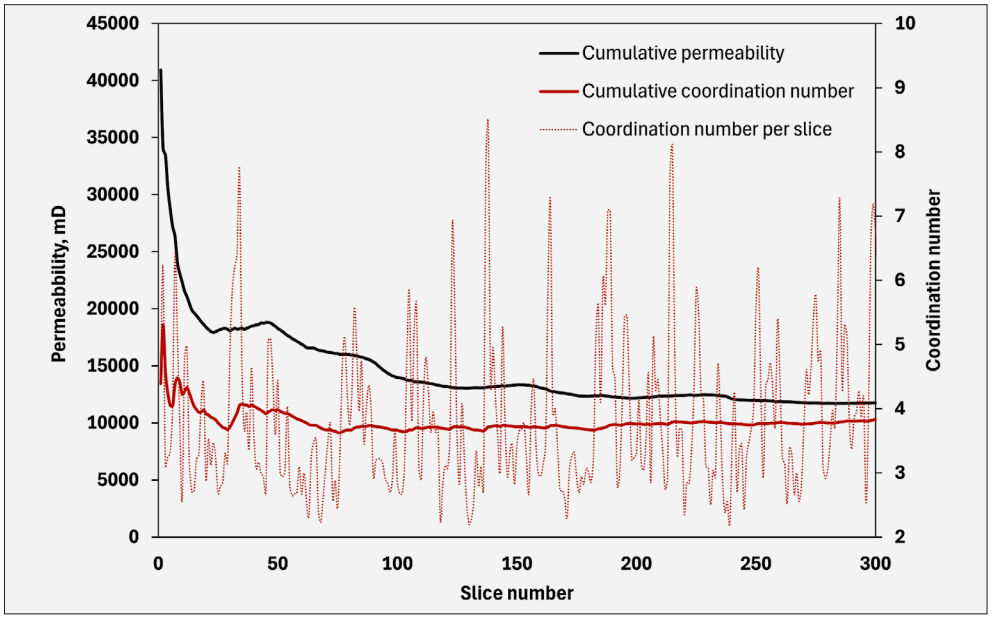


Figure 11: Permeability and coordination number for S8 sample

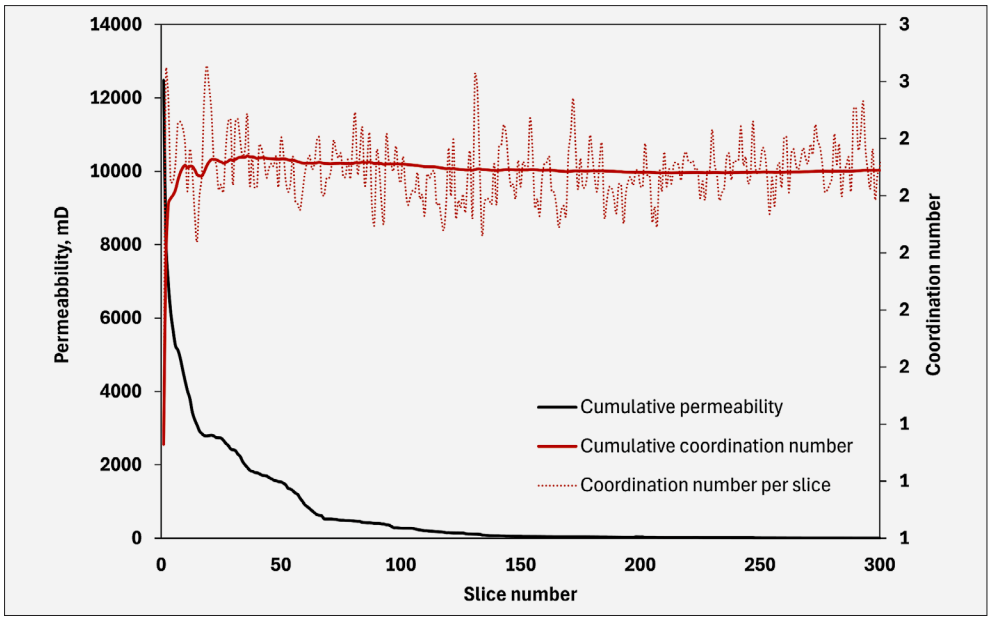


Figure 12: Permeability and coordination number for S4 sample

overlap between connected pores, the same formalism over penalizes constrictions and underrepresents the flow, leading to stronger underestimation and greater sensitivity to voxel size. Overall, geometric characterization supports the view that GMR is best applied in rocks where conductance weighted pore geometry resembles a branched tube network with well resolved throats, and that extensions incorporating explicit overlap areas or *CN* dependent scaling will be needed to extend the method into the tightest, most strongly constricted pore systems.

4. Conclusions

A geometric mean radius (GMR) permeability method was evaluated across a hierarchy of pore geometries, from analytical tube models to micro-CT images of heterogeneous rocks. The method combines a directly measured pore area and a perimeter into a local hydraulic descriptor, propagates conductances through a slice by slice tube network, and aggregates them using explicit rules for series, parallel, and branching connections.

The main findings can be summarized as follows:

- GMR using the hydraulic diameter (scaling factor $M = 2$) reproduces Poiseuille-type behaviour in smooth capillaries and constricted channels, but its accuracy decreases with extreme wall roughness and poor image resolution.
- For well-resolved, highly connected, higher-permeability micro-CT samples, GMR with $M = 1$ yields permeabilities comparable to lattice Boltzmann and grid-based solvers, whereas in tighter, lower-permeability rocks imaged at coarser resolution and exhibiting strong constrictions, GMR tends to underestimate permeability and requires larger multipliers because of small-pore penalization, overlapping cross-sections, and reduced coordination number.
- Analysis of shape factor, circularity, and coordination number confirms that large, irregular pores and well-connected networks favor higher permeability, whereas tight, low-CN systems are more sensitive to imaging limitations and the simplifications inherent in the GMR formulation.
- Significant differences among numerical methods, particularly for low-permeability systems, emphasize the need for laboratory benchmarks and highlight the value of GMR and pore-network approaches for geometric characterization and result validation.

Overall, GMR appears most suitable as a fast, geometrically interpretable permeability estimator for micro-CT volumes where pore throats are well resolved, while future work should focus on overlap-aware weighting, resolution-dependent scaling, and closer integration with pore-network extraction for more complex rocks.

Nomenclature

r_{GM}	geometric mean radius
r_h	hydraulic radius
r_e	equivalent circular radius
D_h	hydraulic diameter
A	pore cross-sectional area
P	pore perimeter
G	shape factor
A_s	cross-sectional area of a model slice
CN	coordination number
k_i	local (individual) pore permeability
k	Sample permeability
M	hydraulic radius scaling factor
τ	tortuosity

Acknowledgement

We would like to express our sincere gratitude to all members of INA d.d., E&P Laboratory, for their patience and understanding during the course of this research. We also acknowledge the provision of equipment and samples that made this work possible. Special thanks are extended to Vjeran Jurković for his innovations and dedication, without which this research would not have been realized.

5. References

Al Khalifah, H., Glover, P. W. J., & Lorinczi, P. (2020). Permeability prediction and diagenesis in tight carbonates using machine learning techniques. *Marine and Petroleum Geology*, *112*, 104096. https://doi.org/10.1016/j.marpetgeo.2019.104096

Ben-Noah, I., Hidalgo, J. J., & Dentz, M. (2024). Pore network models to determine flow statistics and structural controls in variably saturated porous media. arXiv preprint arXiv:2403.13519. https://doi.org/10.1016/j.advwatres.2024.104809

Berg, C. F. (2014). Permeability description by characteristic length, tortuosity, constriction and porosity. Transport in porous media, 103(3), 381-400. https://doi.org/10.1007/s11242-014-0307-6

Bernabé, Y., Mok, U., & Evans, B. (2010). A note on the oscillating flow method for measuring permeability. International Journal of Rock Mechanics and Mining Sciences, 47(5), 784–790. https://doi.org/10.1016/j.ijrmms.2005.04.013

Cai, J., Perfect, E., Cheng, C. L., & Hu, X. (2014). Generalized modeling of fluid transport in porous media: A review. Water Resources Research, 50(9), 6780–6805. https://doi.org/10.1021/la5007204

Carman, P. C. (1937). Fluid flow through granular beds. Transactions of the Institution of Chemical Engineers, 15, 150–166. https://doi.org/10.1016/S0263-8762(97)80003-2

Dong, H. (2008). *Micro-CT imaging and pore network extraction* (Doctoral dissertation, Department of Earth Science and Engineering, Imperial College London).

Dullien, F. A. L. (1992). Porous media: Fluid transport and pore structure (2nd ed.). Academic Press. https://doi.org/10.1016/B978-0-12-223650-1.X5001-3

Foroughi, S., Shojaei, M. J., Lane, N., & Rashid, B. et al. (2025). A framework for multiphase pore-scale modeling based on micro-CT imaging. *Transport in Porous Media,* 152, 18. https://doi.org/10.1007/s11242-025-02156-6

Glover, J. P. W., Zadjali, I. I., & Frew, K. A. (2006). Permeability prediction from MICP and NMR data using an electrokinetic approach. *Geophysics*, *71*(4), F49-F60. https://doi.org/10.1190/1.2216930

Graczyk, K. M., Matyka, M., Khalili, A., & Yilk, D. (2020). Predicting porosity, permeability, and tortuosity of porous media. *Scientific Reports*, 10, 1–12. https://doi.org/10.1038/s41598-020-78415-x

Helland, J. O., Ryazanov, A. V., & Van Dijke, M. I. J. (2008, September). Characterization of pore shapes for pore network models. In *Proceedings of the 11th European Conference on the Mathematics of Oil Recovery (ECMOR XI), Bergen, Norway* (pp. 8-11). https://doi.org/10.3997/2214-4609.20146420

Hommel, J., Coltman, E., & Class, H. (2018). Porosity–permeability relations for evolving pore space: a review with a focus on (bio-) geochemically altered porous media. *Transport in Porous Media*, *124*(2), 589-629. https://doi.org/10.1007/s11242-018-1086-2

Huang, X., Blunt, M. J., & Bijeljic, B. (2020). Validation of pore network modeling for determination of transport properties. *Scientific Reports*, 10, 1–15. https://doi.org/10.1038/s41598-020-74581-0

Kozeny, J. (1927). Über kapillare Leitung des Wassers im Boden [On capillary conduction of water in the soil]. *Sitzungsberichte der Akademie der Wissenschaften in Wien*, *136*, 271–306.

Li, S., Gao, J., Xiao, B., Zhang, Y., Long, G., & Li, Y. (2024). Fractal analysis of dimensionless permeability and Kozeny–Carman constant of spherical granular porous media with randomly distributed tree-like branching networks. *Physics of Fluids*, *36*(6). https://doi.org/10.1063/5.0218990

Mortensen, N. A., Okkels, F., & Bruus, H. (2005). Reexamination of Hagen–Poiseuille flow: Shape dependence of hydraulic resistance in microchannels. Physical Review E, 71(5), 057301. https://doi.org/10.1103/PhysRevE.71.057301

Neumann, R. F., Barsi-Andreeta, M., Lucas-Oliveira, E., Barbalho, H., Trevizan, W. A., Bonagamba, T. J., & Steiner, M. B. (2021). High accuracy capillary network representation in digital rock reveals permeability scaling functions. *Scientific reports*, *11*(1), 11370. https://doi.org/10.1038/s41598-021-90090-0

Rashid, F., Glover, P. W. J., Lorinczi, P., Hussein, D., Collier, R., & Lawrence, J. (2015). Permeability prediction in tight carbonate rocks using capillary pressure measurements. *Marine and Petroleum Geology*, *68*, 536-550. https://doi.org/10.1016/j.marpetgeo.2015.10.005

Rehman, M., Hafeez, M. B., & Krawczuk, M. (2024). A comprehensive review: Applications of the Kozeny–Carman model in engineering with permeability dynamics. Archives of Computational Methods in Engineering, 31(7), 3843-3855. https://doi.org/10.1007/s11831-024-10094-7

Srisutthiyakorn, N., & Mavko, G. (2015, October). An improved kozeny-carman for irregular pore geometries. In *SEG International Exposition and Annual Meeting* (pp. SEG-2015). SEG. https://doi.org/10.1190/segam2015-5914145.1

Srisutthiyakorn, N., & Mavko, G. (2017, September). The revised Kozeny-Carman equation: A practical way to improve permeability prediction in the Kozeny-Carman equation through pore-size distribution. In *SEG International Exposition and Annual Meeting* (pp. SEG-2017). SEG. https://doi.org/10.1190/segam2017-17750852.1

Thomson, P. R., Aituar-Zhakupova, A., & Hier-Majumder, S. (2018). Image segmentation and analysis of pore network geometry in two natural sandstones. *Frontiers in Earth Science*, *6*, 58. https://doi.org/10.3389/feart.2018.00058

Vincens, E., Witt, K. J., & Homberg, U. (2015). Approaches to determine the constriction size distribution for understanding filtration phenomena in granular materials. Acta Geotechnica, 10(3), 291-303. https://doi.org/10.1007/s11440-014-0308-1

Wang, C., Wu, K., Scott, G. G., Akisanya, A. R., Gan, Q., & Zhou, Y. (2019). A new method for pore structure quantification and pore network extraction from SEM images. *Energy & Fuels*, *34*(1), 82-94. https://doi.org/10.1021/acs.energyfuels.9b02522

Xiao, B., Zhu, H., Chen, F., Long, G., & Li, Y. (2023). A fractal analytical model for Kozeny-Carman constant and permeability of roughened porous media composed of particles and converging-diverging capillaries. *Powder Technology*, *420*, 118256. https://doi.org/10.1016/j.powtec.2023.118256

Xiong, Q., Baychev, T. G., & Jivkov, A. P. (2016). Review of pore network modeling of porous media: Experimental and numerical developments. Computers & Geosciences, 88, 79–96. https://doi.org/10.1016/j.jconhyd.2016.07.002

Walker, E., & Glover, P. W. (2010). Permeability models of porous media: Characteristic length scales, scaling constants and time-dependent electrokinetic coupling. *Geophysics*, *75*(6), E235-E246. https://doi.org/10.1190/1.3506561

Wei, M., Cheng, N. S., & Lu, Y. (2023). Revisiting the concept of hydraulic radius. *Journal of Hydrology*, *625*, 130134. https://doi.org/10.1016/j.jhydrol.2023.130134

Zakirov, T. R., & Khramchenkov, M. G. (2020). Prediction of permeability and tortuosity in heterogeneous porous media using a disorder parameter. *Chemical Engineering Science*, *227*, 115893. https://doi.org/10.1016/j.ces.2020.115893

SAŽETAK

Primjena GMR metode za određivanje propusnosti na umjetnim geometrijskim modelima te mikro-CT uzorcima stijena

Propusnost u poroznoj sredini određena je složenom interakcijom morfologije, topologije i povezanosti pora te kritičnih suženja duž tokova fluida na više prostornih razina. U svrhu kvantifikacije međudjelovanja različitih fizičkih utjecaja, razvijena je i testirana metoda geometrijskoga srednjeg radijusa (eng. *geometric mean radius*, GMR) na umjetnim i idealiziranim geometrijama te na modelima stijena dobivenim mikro-CT snimanjem. GMR pristup tretira segmentirani prostor pora kao niz presjeka okomitih na zadani smjer protjecanja te izražava hidraulička svojstva na razini pora iz površine i opsega kombinirajući ih u geometrijski srednji radijus duž povezanih kanala. Serijske i paralelne relacije propusnosti zatim se koriste za propagaciju lokalne vodljivosti pora kroz veze roditelj – dijete, uzimajući u obzir topologiju pornoga prostora, tj. grananje, spajanje i zavojite tokove.
Kontrolirani modeli kapilarnoga tipa koriste se za izdvajanje utjecaja hrapavosti pora, složenosti poprečnoga presjeka, suženja duž toka protjecanja te grananja mreže pora. Procjene propusnosti provedene su za jednostavne geometrije kao i za stvarne uzorke stijena primjenom OpenLB i numeričkih alata dostupnih u softveru PerGeos.
Dodatna geometrijska analiza pornoga prostora pokazuje da ponderirani faktor oblika i koordinacijski broj sustavno koreliraju s propusnošću i s učinkovitošću GMR modela. Rezultati ukupno pokazuju da je GMR računalno učinkovit i geometrijski interpretabilan pristup koji može poslužiti kao alternativa numeričkim simulacijama protjecanja na razini pora, uz primjenu jasno definiranoga raspona povezanosti mreže pora te rezolucije.

Ključne riječi:
propusnost, modeliranje mreže pora, geometrija pornoga prostora, hidraulički radijus, geometrijski srednji radijus

Author's contribution

Marko Gaćina (MSc) developed the conceptual GMR model, extended the initial Python implementation, generated the artificial geometries, performed the numerical simulations, and prepared the manuscript. **Domagoj Vulin** (Professor) developed the GMR Python algorithm for tracking series and parallel permeability and contributed to the conceptualization of the method.
All authors have read and agreed to the published version of the manuscript.